Communications Chemistry

https://doi.org/10.1038/s42004-026-02144-x

Article in Press

Lifetime imaging of singlet oxygen NIR phosphorescence

Received: 27 August 2025

Accepted: 13 July 2026

Published online: 30 July 2026

Cite this article as: Bacellar, I.O., Marques, C.M., Schroder, A.P. *et al.* Lifetime imaging of singlet oxygen NIR phosphorescence. *Commun Chem* (2026). https://doi.org/10.1038/s42004-026-02144-x

Isabel O. L. Bacellar, Carlos M. Marques, André P. Schroder, Carolina Santacruz-Perez, Helena C. Junqueira, Paolo Di Mascio & Maurício S. Baptista

Lifetime imaging of singlet oxygen NIR phosphorescence

Isabel O. L. Bacellar[1†], Carlos M. Marques[2†], André P. Schroder[3], Carolina Santacruz-Perez[1], Helena C. Junqueira[1], Paolo Di Mascio[1], Maurício S. Baptista[1*]

[1]Department of Biochemistry, University of São Paulo, São Paulo, SP, Brazil.
[2]University of Lyon, ENS de Lyon, CNRS UMR 5182, Chemistry Laboratory, 69342, Lyon, France.
[3]CNRS, INSA Lyon, LaMCoS UMR5259, 69621, Villeurbanne, France.

*Corresponding author(s). E-mail(s): baptista@iq.usp.br;
†These authors contributed equally to this work.

Abstract

$^{1}\mathbf{O_2}$ is the first excited state of molecular oxygen and the key intermediate in photosensitized oxidation reactions. Although $^{1}\mathbf{O_2}$ emits near-infrared (NIR) phosphorescence, direct microscopic observation of its emission is severely hampered by its low emission quantum yield, the competitive kinetics between its decay and diffusion, and the limited efficiency of NIR detectors. Here, we describe a $^{1}\mathbf{O_2}$ phosphorescence lifetime imaging microscope ($^{1}\mathbf{O_2}$-PLIM) that allows acquiring lifetime and intensity profiles of $^{1}\mathbf{O_2}$ phosphorescence emission with improved resolution. Calibration carried out with photosensitizer solutions returned the expected lifetimes for $^{1}\mathbf{O_2}$ generation and decay. Nanometer-sized beads allowed the reconstruction of the excitation volume and the estimation of detection limit as 1 million $^{1}\mathbf{O_2}$ molecules in 60 fL of ethanol. Scanning samples in a confocal configuration provided intensity and lifetime image reconstruction of $^{1}\mathbf{O_2}$ emission from complex systems such as micrometer-sized polymer beads bound to photosensitizers, as well as from HaCaT keratynocytes previously incubated with a photosensitizer. Raw image data was corrected for the $^{1}\mathbf{O_2}$ emission lifetime and diffusion pathway within the confocal volume, using a mathematical model specifically developed for this purpose. This advancement in $^{1}\mathbf{O_2}$ imaging enables a better understanding and control of light-mediated reactions across chemistry, biomedicine, and environmental science.

Keywords: Singlet-oxygen microscopy, PLIM, Diffusion-corrected lifetime

1 Introduction

Singlet oxygen $^1O_2$ is the first excited state of molecular oxygen ($^1\Delta_g$) with 94.3 kJ mol^{-1} in excess to its ground triplet state (O_2) [1]. It is usually formed indirectly, by a triplet-triplet energy transfer reaction between the triplet excited states of chromophores, here called photosensitizers (PS), and oxygen [2]. $^1O_2$ is highly reactive towards electron-rich molecules, allowing for the direct oxidation of olefins and biomolecules, initiating the so-called photosensitized oxidation reactions [2–6]. $^1O_2$ modulates several steps of biological signaling, affecting the yield of energy conversion in photosynthesis and the vascular tone during sepsis. It damages biological and man-made surfaces that are exposed to light, such as skin, hair or solar cells. It is also the major intermediate in medical treatments by photodynamic therapy (PDT)[7–13]. However, the precise role of $^1O_2$ in these processes remains elusive for several reasons, including the difficulty in imaging its presence with microscopic resolution.

Several methods have been developed to detect, quantify and study $^1O_2$ [1, 8, 14]. The most acessible methods are based on chemical trapping, typically relying on conventional spectrometry and microscopy setups. Within certain limits and assumptions, these methods allow for identification, quantification and sometimes localization of $^1O_2$ [8, 15]. However, they have two main limitations: (i) accuracy, since the probe's responses are based on the encounter of $^1O_2$ with the probe, which may be fortuitous in complex environments and (ii) specificity, since avoiding parallel reactions with other oxidants is always a challenge [16]. Recently, other techniques have been proposed to avoid these limitations. By assessing the delayed fluorescent emission due to back-energy transfer from the $^1O_2$ to the PS, the probe is the PS itself, localizing only angstroms away from the recently generated $^1O_2$. While the delayed emission can be used to construct images of $^1O_2$ spatial localization, a sophisticated detection scheme is needed in order to separate the delayed fluorescence from the direct fluorescence and phosphorescence emissions of the PS and the obtained image resolution is not ideal [17].

The most specific method for $^1O_2$ detection relies on acquiring its faint but characteristic near infrared (NIR) phosphorescence emission, which peaks at 1270 nm [8, 18]. Time-resolved measurements of this fingerprint emission not only provide tools to discern $^1O_2$ from other emissive species, but also bring insight on the microenvironment of $^1O_2$ molecules [19]. Nonetheless, the photophysical properties of $^1O_2$ create a number of challenges to detect its luminescence: (i) the spectral region where the phosphorescence occurs (i.e. around 1270 nm) has no efficient detector; (ii) the emission is ultra-weak, with intrinsic efficiencies that are among the smallest known (in water, one emitted photon for every 10^8 generated $^1O_2$) and (iii) singlet oxygen lifetimes are in the microsecond domain competing with the diffusion process and complicating the use of available time-resolved photon-counting techniques [20].

Numerous strategies were tried with relative success to image the $^1O_2$ NIR emission [15, 21–27]. Several groups have implemented loupe-type equipment that allows acquisition of $^1O_2$ images with millimeter resolution. These systems have allowed new paradigms in terms of dosimetry in PDT [23–26], but do not provide for microscopic imaging. By using a InGaAs array detector, Andersen and co-workers characterized heterogeneous solvent mixtures with strong contrasts in $^1O_2$ yields in water and in toluene [22]. Few years later this type of detection setup allowed, for the first time, a microscopic observation of the $^1O_2$ phosphorescence emission from a group of cells, which had previously been incubated with TMPyP, which is a standard PS [28]. Scholz and co-workers have further developed this system by using a InGaAs 2D-array detector to allow image and spectral resolution within the same sample acquisition [26]. However, the quality of the images were never good enough to allow improvements in the field.

Obtaining precise values of the $^1O_2$ lifetime in complex environments continues to challenge the scientific community, as such information is crucial for understanding the diffusion, reactivity, and site-specific oxidative damage induced by photosensitizers (PS) [29]. The pioneering work of Ogilby's group established the field of singlet oxygen microscopy, first by measuring $^1O_2$ kinetic profiles from single cells [15, 30] and later by achieving phosphorescence lifetime measurements in subcellular domains [31, 32]. NIR signals from cell suspensions also were used to evaluate the intracellular dynamic decay of singlet oxygen [15, 20, 33–35]. The field of singlet oxygen detection in the microscopic domain has been recently reviewed [36]. A key technological advance was reported by Tian et al., who demonstrated the first full-field singlet oxygen phosphorescence lifetime imaging microscope (SOPLIM) by modifying a commercial FLIM system, proving the feasibility of simultaneous intensity and lifetime mapping, albeit in a solid-state sample [37].

Here, we build upon this principle by developing a highly sensitive phosphorescence lifetime imaging microscope based on a single-molecule FLIM platform, approaching the sensitivity needed for single-cell analysis. By integrating a scanning objective, subpicosecond laser excitation, and ultra-sensitive detectors, coupled with theoretical modeling, we achieve a dramatic improvement in detection sensitivity. While Tian et al., system relied on stage-scanning configurations with infrared-incompatible optical components, leading to significant signal attenuation and limited spatial resolution [37], our developed $^1O_2$-PLIM system employs a dedicated, optimized optical path that includes a near-infrared (NIR) photomultiplier tube, a 1270 nm long-pass filter, and a silicon-immersion objective, all integrated into a laser-scanning confocal architecture with a piezo stage. Our setup also incorporates a time-gated excitation scheme that temporally separates the photosensitizer emission from the phosphorescence, allowing for unambiguous detection of the weak 1270 nm signal. This tailored instrumentation overcomes the key limitations of prior adaptations, enabling confocal, time-resolved imaging of singlet oxygen with micrometer spatial resolution.

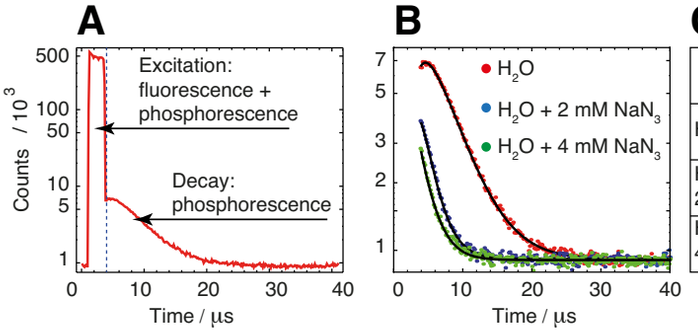

	τ_1 / µs	τ_2 / µs
H_2O	3.6±0.1	1.7±0.1
H_2O + 2 mM NaN_3	0.6±0.1	1.9±0.1
H_2O + 4 mM NaN_3	----------	1.9±0.1

Fig. 1 Example of a full NIR decay profile. Here methylene blue ($\lambda_{exc} = 640$ nm) is employed as a photosensitizer to generate $^1O_2$ in water in the absence and in the presence of sodium azide (NaN_3). (A) Excitation region has a square shape followed by the usual $^1O_2$ decay. (B) $^1O_2$ phosphorescence fitted by biexponential functions with (C) the corresponding fit values where τ_1 and τ_2, are the $^1O_2$ and triplet-state lifetimes, respectively.

2 Results

Detecting $^1O_2$ emission with the phosphorescence lifetime imaging microscope ($^1O_2$-PLIM)

The $^1O_2$-PLIM, see below the Equipment paragraph of the Methods section, was designed by us and constructed by PicoQuant (Berlin, Germany). PicoQuant adapted its single molecule fluorescence microscope (MicroTime 200) to allow acquisition and imaging of $^1O_2$-phosphorescence. Both the excitation in the visible and the detection in the NIR were properly time-gated and the optical parts (lenses, dichroic and filters) were selected to allow efficient collection of NIR photons coming from the $^1O_2$ phosphorescence (further details can be found in the Methods). To confirm the detection of $^1O_2$, initial measurements were carried out by exciting homogeneous solutions of methylene blue (MB), which is a typical $^1O_2$ PS. Data acquisition was performed in a random fixed position of the objective and the typical cycle of excitation/emission can be observed in Fig. 1*A*. Excitation was performed with 200 pulses of a 640 nm pulsed laser of 20 ps (full width at half maximum, FWHM) and the NIR light acquisition was performed in the NIR-PMT as a function of time (see SI for further information). Fig. 1*B* shows emission decays in water with or without sodium azide, which is a known quencher of $^1O_2$. Decays (Fig. 1*B*) fitted with the appropriate combination of exponential functions [15] yielding the expected values (Fig. 1*C*) for MB's triplet excited state lifetime and also for $^1O_2$ lifetimes in the absence of quencher, i.e. 1.7 μs and 3.6 μs, respectively [38, 39]. The addition of sodium azide decreased the $^1O_2$ lifetime up to a point where only the MB triplet excited state lifetime could be extracted from the decays (Fig. 1*B*) and (Fig. 1*C*).

NIR emission signals were also characterized from rose bengal (RB) aqueous solutions, prepared in the absence or in the presence of an excess of the protein BSA, a condition in which the PS is totally bound to the BSA and does not generate any $^1O_2$ [40]. Note that RB excitation in aqueous solution generates the characteristic $^1O_2$ decay (lifetime of 3.9 μs), while when bound to BSA, the signal drops instantaneously

after excitation is stopped. Therefore, it is possible to acquire $^1O_2$ NIR signals, excluding other light-induced processes, such as the direct fluorescence and phosphorescence from the PS and the sample light scattering, by only analyzing emission signals after the laser pulses have ended (see below the Methods section).

Sensitivity measurements

In order to determine the limit of detection (LOD) of $^1O_2$-PLIM, ethanol solutions of two different photosensitizers, MB and RB, were used for calibration purposes (see also below the Methods section). In both cases, excitation volumes were $\sim$ 60 femtoliters and the LOD with respect to photosensitizer concentration was in the submicromolar concentration range. This corresponds to a limit of detection of several $\sim 10^3$ molecules of $^1O_2$ generated in the confocal volume per excitation cycle, measured over 60 s to a total of generated $\sim 10^9$ $^1O_2$. Over the measurement duration a total of a few tens of thousand of IR photons are emitted, from which a few percent are counted by $^1O_2$-PLIM (see *Limits of detection* in Methods). This detection capability is comparable to the efficiency reported by Niedre et al. [34], which nevertheless relied on a macroscopic detection configuration, i.e., volumes of 300 μL (nine orders of magnitude larger than our excitation volume). The sensitivity also compares favorably with pioneering microscope-based $^1O_2$ detection: for example, early two-photon microscopy work achieved detection from $\sim$10 fL volumes in non-aqueous solvents, but noted significant challenges in obtaining reliable signals from aqueous systems or single cells [41]. Therefore, we aim to combine the high sensitivity previously associated with macroscopic detection with the spatial resolution of microscopy, enabling robust $^1O_2$ imaging from microscopic volumes in biologically relevant environments, including single cells.

Imaging capability of the $^1O_2$-PLIM

To demonstrate the potential of the $^1O_2$-PLIM equipment to acquire and construct images from $^1O_2$ emission decays, we analyzed the emission profile of single Sensitox® beads, which are 200-400 mesh polysterene beads bound to Rose Bengal, in the visible (Vis) and NIR regions (excited at 510 nm), when they were suspended in different media (Fig. 2), see Materials. Besides the optical tools used to select $^1O_2$ in the $^1O_2$-PLIM equipment (see Methods), $^1O_2$ phosphorescence emission was also temporally selected from other signals, by disregarding all photons collected during excitation pulses, as exemplified in Fig. 1 *A*. Sample was scanned by moving the objective and phosphorescence decays at 1270 nm were collected pixel-by-pixel (see Methods). Images can be constructed with intensity (at any point in the time curve) and lifetime data, or both. When suspended in air, it is possible to observe that the images constructed purely with the values of maximum intensity per pixel in the vis and NIR regions are somewhat different (Figs. 2 *A* and 2 *B*, for Vis and NIR, respectively). Although both images were acquired from the same bead, the radial intensity profile of the Vis image exhibits a more gradual decay compared to the corresponding NIR profile, as shown in Fig. 2.C as blue and red curves. Note that the Vis image has almost constant emission up to 15 μm, while the NIR image start to lose intensity below 10

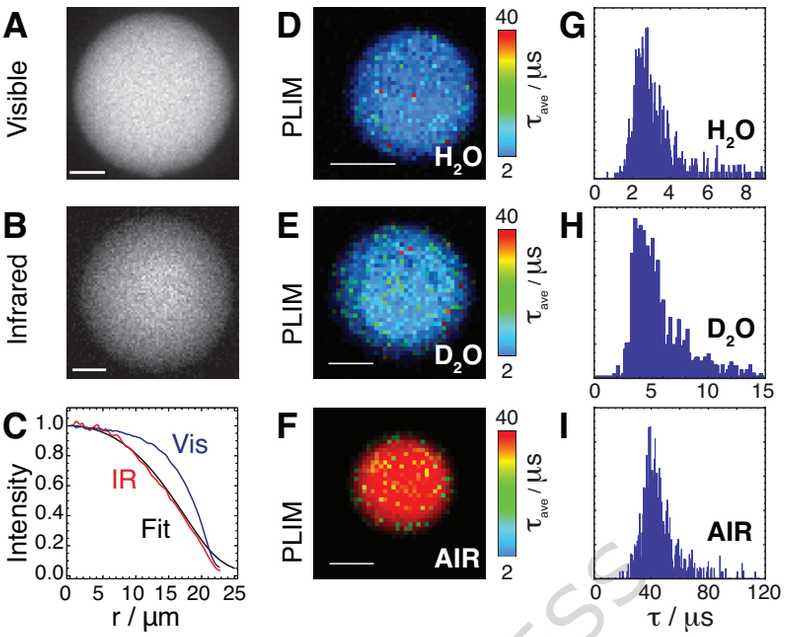

Fig. 2 Images of Sensitox® particles. A) particles imaged in air in the visible and B) particles imaged in air in the NIR ranges. Their normalized radial intensity profiles are shown in C), with the predicted IR profile in black computed from the instrument parameters and the sensitizer distribution. D, E and F show phosphorescence lifetime images of Sensitox® in H_2O, D_2O and air, respectively. To optimize visual contrast for representation, the display intensity was scaled from 20% (black) to 80% (white) of full pixel intensity range, with no other image processing applied. All quantitative analyses were performed on the raw, unmodified data. The average lifetime (τ_{ave}) is represented by color coding (scale to the right). Intensity-weighted lifetime distribution histograms are also shown for G) H_2O, H) D_2O and I) air, for the same particles. Scale bars are 20 μm.

μm, having therefore a larger spread. As further explained below, such spreading is due to a combination of the longer lifetime and higher mobility of $^1O_2$ (emitting in the NIR) compared with the shorter lifetime and smaller mobility of the singlet excited state of RB (fluorescence emission in the Vis). The mathematical model developed to treat the raw data acquired from the $^1O_2$-PLIM, accounts for both lifetime and diffusion effects in the confocal volume, as explained further below.

Images were also constructed considering intensity and lifetime (PLIM) profiles from beads immersed in two condensed media, i.e., H_2O and D_2O, Fig. 2.D and 2.E, respectively, besides air (Fig. 2.F). The bar code at the right side of Figures 2D, E and F provides the color codes for lifetime, and the respective lifetime histograms are plotted in figures 2 G, H and I. The measured lifetimes are distributed over a range of values and should be interpreted qualitatively. The key finding is the clear distinction between different environments, with the average $^1O_2$ lifetime increasing in the order $H_2O < D_2O <$ air ($2.5 < 5 < 40$ μs, respectively), consistent with expectations, although the absolute values are representative of the specific experimental conditions [39]. For instance, the lifetime measured in air reflects the ambient laboratory conditions (approximately 60% relative humidity), where water vapor acts as a known

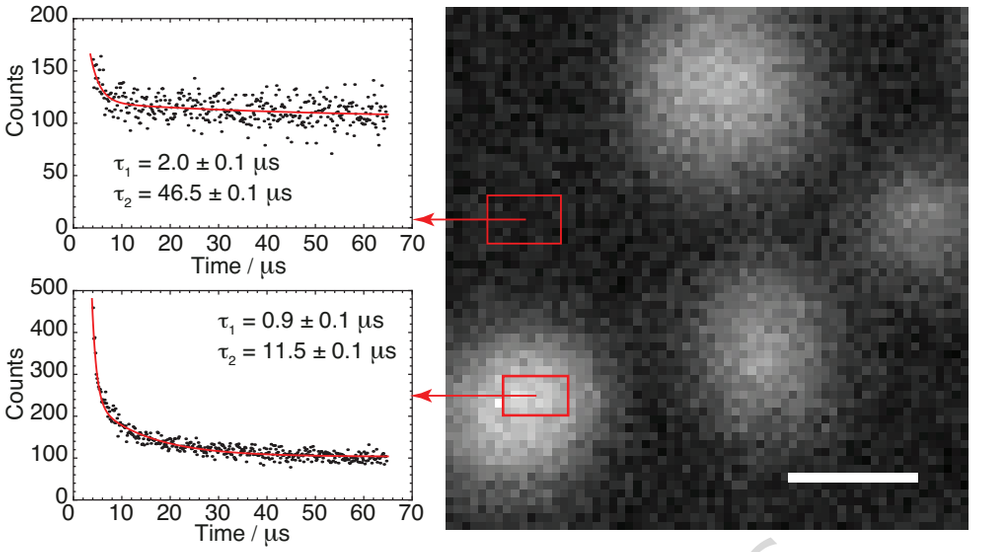

Fig. 3 Phosphorescence emission of HaCaT cells previously incubated with RB 1μm. Left panels: NIR decays in the regions without cell (upper graph) and with cell (lower graph). Right panel: Image construction from pixel-by-pixel $^1O_2$ emission. Scale bar is 20 μm.

quencher. Similarly, the value in D_2O is affected by H/D exchange with residual water in the beads and the atmosphere. The shorter lifetime portions of the histogram are possibly associated with the population of $^1O_2$ molecules that are quenched by the particles themselves[10]. Importantly, the figures show that $^1O_2$ lifetimes are independent of the radial coordinate, indicating that the Sensitox® bead matrix does not generally suppress $^1O_2$. These results demonstrate that our $^1O_2$-PLIM setup can reliably resolve differences in singlet oxygen microenvironments and properly reconstruct images of $^1O_2$ emission with microscopic resolution.

The observed singlet oxygen lifetime of approximately 40 microseconds in air at 60% relative humidity is consistent with established quenching dynamics, where the long radiative lifetime in dry air is drastically shortened by water vapor. Using the quenching rate constant for water vapor $k_{H_2O} = 1.8 \times 10^3$ s^{-1} Torr^{-1} [42] and the partial pressure of water at 60% RH (14.3 Torr at 25°C), the calculated lifetime is 39 microseconds, in good agreement with our measurement. Furthermore, the shorter lifetime of 5 microseconds observed in D_2O with Sensitox® beads, compared to 11.5 microseconds in cellular experiments, is quantitatively explained by atmospheric H_2O contamination: the exposed D_2O droplet equilibrates with ambient moisture (60% H_2O mole fraction), yielding a calculated lifetime of 5.2 microseconds. Thus, both values are rationally explained by the dominant quenching effect of water vapor under the respective experimental conditions.

Imaging cells

To test the performance of this equipment to detect and imaging $^1O_2$ inside cells, we performed experiments in HaCaT cells previously incubated with 1 μm of Rose

Bengal in D_2O (Fig. 3) [43]. Notably, cell boundaries become evident when image is reconstructed from the $^1O_2$ signals. Emission from within HaCaT cells is roughly three times stronger than the emission signals coming from the external medium. This represents a significant improvement in spatial resolution for intracellular $^1O_2$ imaging at the micrometer scale compared to earlier methodologies (see Fig. 9 in reference [44], Figs. 6-8 in reference [26] and Fig. 2 in reference [28]), allowing for clearer visualization of the spatial distribution of $^1O_2$ within cells.

In contrast to earlier singlet oxygen microscopy studies that reported sensitizer bleaching as a significant concern during image acquisition [44], we did not observe evidence of this effect in our PLIM experiments. We attribute this to key differences in our excitation protocol. Our setup employs picosecond, time-gated laser pulses followed by long dark periods, resulting in a low average power at the sample, as described in the Limits of Detection paragraph.

The fact that each pixel carries lifetime information allowed us to also interrogate the $^1O_2$ lifetimes within the cells. Emission profiles from the red-delimited regions (Fig. 3) were averaged and fitted to a double-exponential function. Inside the cell, the two lifetime components (0.9 μs and 11.5 μs) likely reflect the heterogeneous intracellular environment, where singlet oxygen encounters distinct micro-domains with different quenching efficiencies. Outside the cell, the decay also required a double-exponential description (2.0 μs and 46.5 μs). While the average lifetime in this region is consistent with that expected for a H_2O/D_2O mixture, the biexponential character probably arises from residual sample heterogeneity (e.g., local variations in solvent composition, surface-adsorbed layers, and biomolecules coming from the cells) rather than from two independent bulk-solvent quenching pathways.

Nevertheless, our data (Fig. 3) clearly shows that the intracellular environment quenches both the short and long $^1O_2$ lifetimes. By analyzing kinetic profiles of NIR emission from cells, independent groups reported that $^1O_2$ lifetimes present in the intracellular domain are considerably smaller from those obtained in bulk solutions. Cells in aqueous suspensions showed $^1O_2$ decays in the microsecond to sub-microsecond domains [20, 33, 34]. Previous work by others and by us, also reported shorter lifetimes of $^1O_2$ in cells suspended in D_2O [15, 35, 45]. Even though others have reported transient singlet oxygen emission from cells, we advocate that, as shown in Fig. 3, our equipment improved the spatial resolution of the cellular visualization.

Obtaining precise values of the $^1O_2$ lifetime in complex environments continues to challenge the scientific community. Information concerning the diffusion and reactivity of $^1O_2$ in cells is crucial for understanding the relationship between the intracellular site of photosensitizer (PS) localization and the sites of oxidative damage [29]. Pioneering work by Ogilby's group, using microscopy to collect $^1O_2$ phosphorescence from single cells, reported that $^1O_2$ lifetimes were not heavily quenched in the intracellular domain under their specific experimental conditions [15, 30]. In contrast, the majority of studies acquiring NIR signals from bulk cell suspensions, which average the signal over the entire heterogeneous cellular volume, converge on the conclusion that $^1O_2$ lifetime is significantly shortened in the intracellular environment [15, 20, 33, 34]. Our data, obtained with confocal $^1O_2$-PLIM, support the interpretation that singlet oxygen is quenched in the intracellular environment. The biexponential decay we observe

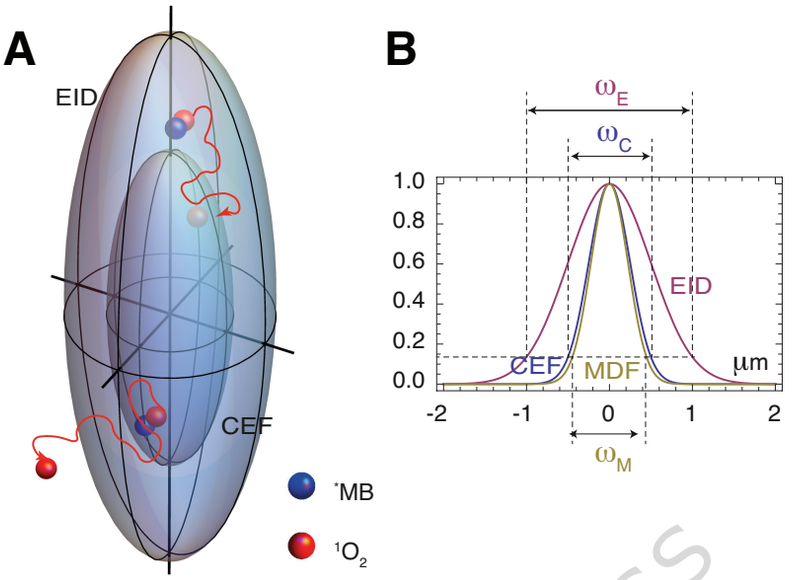

Fig. 4 Schematic representation of the bias introduced into the decay function of $^1O_2$ phosphorescence by diffusion. A) 3D representation of the excitation and collection volumes, and of two typical trajectories of $^1O_2$. When $^1O_2$ decays inside the collection volume its photon is collected, otherwise it is lost. B) The excitation and collection volumes are defined respectively by the region in space where the excitation intensity distribution (EID) and the collection efficiency function (CEF) have values larger than a fraction $e^{-2} \simeq 0.135$ (horizontal dashed line) of their respective maxima. The so-called confocal volume, defined similarly from the molecular detection function (MDF) can be measured experimentally, see below for a measurement of the MDF in our detection geometry.

inside cells (Fig. 3), featuring a major short-lived component (0.9 μs), is consistent with the rapid quenching expected in a biomolecule-rich environment. While a longer component (11.5 μs) is also present, it is also much shorter than the lifetime expected for $^1O_2$ in bulk D_2O [18]. Critically, the average lifetime and the dominant kinetic behavior align more closely with the results from cell suspension studies [33, 34], which reflect the bulk intracellular environment where interactions with proteins, lipids, and other cellular constituents are a significant factor in $^1O_2$ deactivation. Indeed, the observed solvent H/D isotope effect (shorter lifetime in H_2O than in D_2O) and the efficient quenching by added sodium azide [15] indicate that intracellular water also plays a key role in deactivating singlet oxygen, kinetically competing with biomolecules. Therefore, our work reinforces the model that the intracellular lifetime of singlet oxygen is not only determined by biomolecules but also, importantly, by water, which is a key suppressor of $^1O_2$ under physiological conditions.

Influence of diffusion on phosphorescence lifetime measurements: computing the detection of $^1O_2$ emission in confocal volumes

Our detection geometry is that of a standard confocal experiment. The emissive molecule is excited inside the so-called excitation volume, roughly a prolate ellipsoid defined by the region of the excitation intensity distribution (EID) where the excitation light beam is intense, see Fig. 4*A*. The ellipsoid has two short semi-axes in the (XY) plane of length w_E and one long (Z) axis of length $k_E w_E$, with $k_E > 1$. In such geometry, emitted photons are collected with an efficiency described by the collection efficiency function (CEF), also defining a collection ellipsoidal volume of semi-axes w_C and $k_C w_C$. The molecular detection function (MDF) describing the light distribution collected from an excited point-like emissive molecule is given by the product of the EID and of the CEF. If all distributions are conveniently approximated by Gaussian functions, the so-called confocal volume associated with the MDF is also an ellipsoid, with short and long semi-axes given by $w_M^{-2} = w_E^{-2} + w_C^{-2}$ and $k_M^{-2} w_M^{-2} = k_E^{-2} w_E^{-2} + k_C^{-2} w_C^{-2}$. By imaging small fluorescent particles with sub-optical dimensions we mapped the MDF for our observation conditions obtaining $w_M = 0.5$ μm and $k_M = 4$, see also below for the measurement of these quantities. We express the CEF and EID dimensions as a function of the two measured values for w_M and k_M by introducing the relative extensions of the CEF and EID in the XY and Z directions, respectively $\alpha = w_C/w_E$ and $\beta = k_C w_C/(k_E w_E)$, see also Fig. 4. Although we cannot directly measure α and β, analysis below indicates that for our case $\alpha = \beta = 0.3$, that is the semi-axes of the excitation volume are three times larger than those of the collection volume.

It is crucial to contextualize these volumetric dimensions with the theoretical diffraction limit, which sets a fundamental lower bound for the spatial resolution of our optical system. The measured lateral dimension of the Molecular Detection Function, $w_M = 0.5$ μm, is consistent with a diffraction-limited spot for our high Numerical Aperture (NA=1.05) objective and visible light detection. However, the excitation volume (V_E) and collection volume (V_C) are distinct concepts. The excitation volume, where photons are absorbed, is defined by the focused laser spot and is inherently diffraction-limited. The collection volume, from which emitted photons are efficiently detected, is also constrained by diffraction but is characterized separately by the CEF. The key insight for singlet oxygen imaging is that the effective spatial origin of the 1270 nm phosphorescence signal is not confined to these diffraction-limited volumes. Due to the microsecond-scale lifetime of $^1O_2$, molecules diffuse significant distances (hundreds of nanometers) between excitation and emission. This means the effective resolution of a $^1O_2$-PLIM image is not solely determined by the diffraction limit of the optics but is also governed by the diffusion length of $^1O_2$ during its lifetime. Our model, which explicitly separates the EID and CEF, is essential for correctly interpreting the measured lifetimes and intensity distributions in this context, where the signal from a single confocal voxel inherently contains information from a dynamically enlarged region.

Given the short lifetimes of fluorescent excited states ($\tau \sim 10^{-9} - 10^{-8}$ s), even fluorophores with large diffusion coefficients ($D \sim 10^{-8}$ m^{2}s^{-1}) only explore distances

of the order of a few nanometers $\sqrt{D\tau} \sim 3-10$ nm: in practice, a fluorophore excited within the excitation volume emits for all detection purposes from the same location. For a long-lived phosphorescent species such as $^1O_2$, typical decay times τ are in the order of 10^{-5} s. The excited oxygen species can thus travel over distances of 300 nm or more. $^1O_2$ species created in the excitation volume have thus a finite probability of being detected far from the excitation location or to exit the detection volume before they decay, as depicted in Fig. 4A. Potentially this can impact both the measured decay functions and the PLIM images. Importantly, an intrinsically exponential decay process can give rise to a detected decay function that will not only decay faster than expected but also exhibit a non-exponential form as discussed below. Moreover, $^1O_2$ mobility will also modify the contrast in microscope images, a modification extensively discussed below.

By properly accounting for diffusion, we show below in the *Quantitative description of lifetime imaging for long-lived emission processes* section in Methods that the expected diffusion biased decay function (DBDF), *i.e.* the number of photons emitted at time $t > -t_{ex}$ by emissive molecules excited by laser pulses following some excitation function $f(t)$ between times $-t_{ex} < t < 0$ can be written as

$$\mathrm{DBDF}(t) = \int_{-t_{ex}}^{0} dt' f(t') \left[1 + \frac{8(t-t')}{\tau_M(\alpha^{-1}+\alpha)^2}\right]^{-1} \times \left[1 + \frac{8(t-t')}{k_M^2\tau_M(\beta^{-1}+\beta)^2}\right]^{-1/2} \exp\{-\frac{t-t'}{\tau}\} \quad (1)$$

where the confocal residence time τ_M, the time that the mobile probe spends in the confocal volume is given by $\tau_M = w_M^2/D$ (see also Fig. 4). Table 1 shows the decay times obtained by fitting the $^1O_2$ decay data in homogeneous ethanol and D_2O solutions (Fig. 1*C*) with classical bi-exponential fitting and with Eq. 1, where we used $\alpha = \beta = 0.3$, the measured value $k_M = 4$ and a residence time $\tau_M = 100$ μs obtained from the measured confocal volume size $w_M = 0.5$ μm and the oxygen diffusion coefficient $D = 2.5 \times 10^{-9}$ m^2.s^{-1}. Note that both treatments provide good data fittings (see fitting residues at the end of the paper), but the lifetime values extracted from the DBDF are more accurate [39].

Table 1 Lifetimes of singlet oxygen luminescence in liquids in μs obtained by fitting the decays with biexponential and with DBDF forms.

Solvent	Biexponential	DBDF	Literature
1. D_2O	52.8 ± 0.4	62.0 ± 0.5	60-65
2. Ethanol	13.5 ± 0.2	14.2 ± 0.3	14-15

Within the same framework we used Eq.16 to fit the IR radial (red) profile in Fig. 2*C*. As the figure shows, by taking as input for the radial sensitizer distribution $O(r)$ the Vis radial profile (blue) from Fig. 2 *C*, a good fit (black) is obtained with the same geometrical values $\alpha = \beta = 0.3$ as above, a residence time $\tau_M = 0.01$

μs obtained from the measured confocal volume size $w_M = 0.5\ \mu m$ and the oxygen diffusion coefficient in air $D = 2.5 \times 10^{-5}\,\mathrm{m^2.s^{-1}}$ and the measured value of $^1O_2$ decay time in air $\tau = 50\ \mu$s, see Fig. 2*I*.

Concluding remarks

As others had achieved before, we also accomplished microscopic resolution in the detection of time-resolved NIR phosphorescence images of $^1O_2$ emission. We argue that the combination of improved microscopic set up together with the development of a theoretical model allowed an important improvement in the field. We successfully achieved microscopic resolution in the detection of time-resolved NIR phosphorescence images of $^1O_2$ emission. By overcoming key challenges - such as the ultra-weak NIR phosphorescence signal, competing diffusion-decay kinetics, and detector inefficiencies - our system enables direct visualization of $^1O_2$ localization and lifetime dynamics in complex environments. Calibration with photosensitizer solutions and nanometer-sized beads confirmed the system's sensitivity, detecting as few as 1 million $^1O_2$ molecules in a 60-femtoliter volume. The integration of a mathematical model to correct for lifetime and diffusion artifacts further enhances the accuracy of spatial and temporal $^1O_2$ profiling. The new theoretical development can be used for the confocal detection of any long-lived mobile emitting species. Applications in HaCaT keratinocytes incubated with photosensitizers demonstrate the method's versatility, providing insights into $^1O_2$ behavior at the cellular level.

The $^1O_2$-PLIM platform bridges a critical gap in understanding $^1O_2$-mediated processes, from photodynamic therapy to material degradation. By correlating $^1O_2$ lifetime variations with microenvironmental properties, this work lays the foundation for future studies on reactive oxygen species dynamics in biological, medical, and materials science contexts. The proof-of-principle established here will drive the development of next-generation instrumentation, offering unprecedented resolution to unravel how light-driven oxidation impacts diverse systems. This technological development promises to refine therapeutic strategies, optimize photochemical applications, and deepen fundamental knowledge of $^1O_2$'s role in natural and engineered systems. Our approach provides a new strategy for $^1O_2$ detection, a new tool for better understanding the role that this reactive species plays in the many processes where oxidation occurs when light interacts with matter.

3 Methods

Equipment

The layout of our equipment, depicted in Fig. 5, is based on a MicroTime 200 fluorescent time-resolved microscope from PicoQuant (Berlin, Germany). The equipment was adapted for $^1O_2$ detection by including a NIR phosphorescence channel. NIR detection was performed by a thermoelectrically cooled NIR photomultiplier tube detector (PMT) from Hamamatsu (H10330B) and by making other changes: (1) a silicon-immersion Olympus UPlanSApo IR 30x/1.05 objective was mounted on a piezo scanner in an IX73 Olympus inverted microscope; (2) a major dichroic, reflecting light

below 950 nm (950dcxrxt, Chroma), was placed inside the main optical unit; a 1.5 mm pinhole was employed in order to enhance sensitivity; (4) a 1270 long pass filter (Thorlabs) was placed before the PMT. Pulsed diode lasers with wavelengths of 640 and 510 nm (LDH Series from PicoQuant) were used to excite MB and RB (free or polymer-bound), respectively. The excitation program was generated by the system software of the PDL 828 "Sepia II" laser driver (PicoQuant). It consisted of 200 laser pulses of 20 ps full width at half maximum at a repetition rate of 80 MHz (one pulse every 12.5 ns during 2.5 μs), followed by a pause of variable length (1000-10000 pulses, set according to $^1O_2$ lifetime), a synchronization signal and an additional pause (100 pulses). All other microscope components were controlled by the SymPhoTime 64 software (version 2.0, PicoQuant). Time transient histograms were acquired by using Time Correlated Single Photon Counting (TCSPC). Decay transients were obtained by scanning the objective through the sample, pixel by pixel. Images were constructed by integrating the time decays in the chosen sample space.

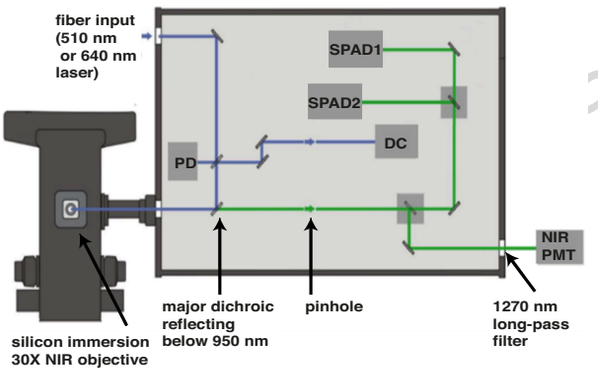

Fig. 5 Layout of the confocal microscope for $^1O_2$ detection. Abbreviations: PD (photodiode detector), DC (diagnosis camera), SPAD (single photon avalanche detector), NIR PMT (near-infrared photomultiplier tube detector). Figure adapted from the original scheme of the Picoquant's MT200's equipment, considering the modifications implemented for this study.

Materials

Sodium azide and deuterium oxide (D_2O), and the photosensitizers (PS) methylene blue (MB) and rose begal (RB), were acquired from Sigma-Aldrich. Ethanol was acquired from Synth. Sensitox® beads (CAS 9403542-4), made from chloromethylated polystyrene-divinylbenzene copolymer modified with RB, were acquired from Hydron Laboratories, Inc., Brunswick, New Jersey. Tetraspeck beads were acquired from ThermoFischer. All aqueous solutions were prepared with Milli-Q water (Millipore).

$^1O_2$ in aqueous and BSA solutions

We performed $^1O_2$ emission experiments with rose bengal (RB) solutions with and without the protein BSA. According to [40] in the absence of BSA, RB leads to $^1O_2$ formation and very weak fluorescence. Upon addition of BSA, fluorescence increases and $^1O_2$ generation decreases significantly or vanishes, because RB binds to the hydrophobic pocket of BSA, making the encounter with oxygen unfeasible. Indeed, as shown in Fig. 6 in the presence of BSA, only the square emission acquired during excitation is observed, and as soon as the excitation cycle ends, there is no more emission, indicating that the square signal during the excitation cycle is not due to $^1O_2$ emission. Nevertheless, in the absence of BSA, after the excitation signal ends, RB generates a clear $^1O_2$ signal. Despite a significant noise, fit of this signal accounting for both triplet and $^1O_2$ lifetimes gives respectively 2.5 μs and 3.9 μs close to measured RB values in water.

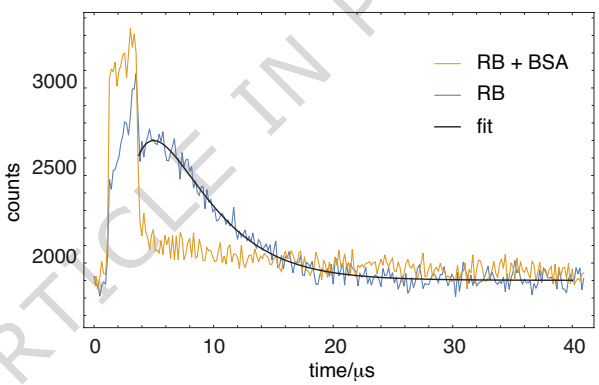

Fig. 6 NIR Emission Transient of Rose Bengal solution (10 μM) in Tris Buffer (20 mM, pH =7.3) in the absence and presence of BSA (3.3 mM), excitation at 510 nm. The excitation protocol (described in Methods) is not a continuous 2.5 μs light pulse. It consists of 200 individual laser pulses at 80 MHz (12.5 ns between pulses). Each pulse is extremely short (20 ps FWHM). This creates a 2.5 μs window containing a train of discrete, picosecond excitation events. For lifetime analysis, all photons detected during this entire excitation window are deliberately discarded ("time-gated"). The analysis only considers photons arriving after the last laser pulse in the burst. Therefore, the 2.5 μs duration of the excitation train does not limit the ability to measure a decay that starts immediately after it ends.

Limits of detection (LOD)

$^1O_2$ luminescence profiles were acquired during 60 seconds in ethanol following the excitation sequence introduced above repeated 465972 times (every (200+10000+1+100)×12.5 ns = 128 763 ns) for MB (λ_{ex}=640 nm) or 761 784 times, every (200+6000+1+100)×12.5 ns = 78 762.5 ns for RB (λ_{ex}=510 nm). Mono-exponential curves were fitted to the data and the exponential prefactor A_1, corresponding to the number of 1270 nm photons collected during 60 s, was plotted as a function of PS concentration, see Fig. 7. For both MB and RB sensitizers the calibration curves could be well fitted ($R^2 > 0.99$) by straight lines passing through the

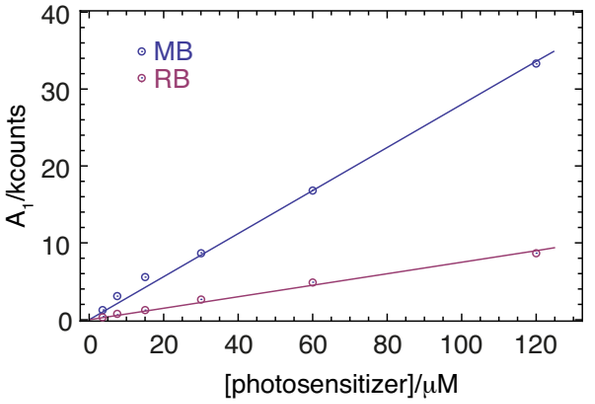

Fig. 7 Calibration curves of the intensity of singlet oxygen luminescence (taken as the exponential prefactor A_1 for mono-exponential decays) as a function of MB or RB concentration in ethanol solutions. Excitation was λ_{ex}=640 nm λ_{ex}=510 nm, respectively. Standard deviations are always smaller than symbol sizes.

origin. The LOD in terms of PS concentration (LOD_{PS}) was calculated as the amount of PS required to reach an intensity equal to three times the mean standard deviation of the signal at the very end of singlet oxygen decays for the set of the decays used to build the calibration curve. One gets $LOD_{MB} = 0.2$ μM and $LOD_{RB} = 0.9$ μM as displayed in Table 2. The LOD_{PS} concentrations correspond to 266 MB molecules or 607 RB molecules within the confocal volume, see also Table 2. From the total number of IR (1270 nm) photons that are emitted in the confocal volume following PS excitation, our configuration detected 5325 IR photons from MB excitation and 6656 from RB excitation, determined by summing all photons over the exponential decay. We now determine the ratio of IR photons detected to IR photons emitted.

Table 2 Limits of detection for photosensitizer molar concentration (LOD_{PS}) and photosensitizer number $LOD_{\#}$=$LOD_{PS} \times V_M$ with the confocal volume $V_M = 4\pi/3 k_M w_M^3$, see below for measured dimensions. At this concentration limit, 60 s of excitation cycles create a number $LOD_{^1O_2}$ of singlet oxygens that decay into LOD_{IR} infrared (1270 nm) photons, a fraction of them are detected by the instrument.

	LOD_{PS} μM	LOD_{PS} #	$LOD_{^1O_2}$ #	LOD_{IR} emitted	$LOD_{\#IR}$ detected
MB	0.2	266	5.01×10^9	24061	5325
RB	0.9	607	1.15×10^10	55438	6656

The light beam power values for each experimental condition were quantified by placing an OP2-Vis detector of a Fieldmate (Coherent) power meter in front of the objective, and converted to the average power of the excitation sequence by assuming that the power meter reading results from the time average of the pulse

sequence. More precisely, we followed an excitation sequence as described above with a pause of 6000 pulse intervals. The power-meter reading in Watts is multiplied by (200+600+1+100)/200 to provide average powers of 3.06 mW (λ_{ex}=640 nm) and 0.93 mW (λ_{ex}=510 nm) during the excitation interval of 2.5 μs. Further multiplying by the pulse interval of 12.5 ns to give 38.28 pJ per pulse for λ_{ex}=640 nm and 11.62 pJ per pulse for λ_{ex}=510 nm.

The excitation frequency Q_{PS} of photosensitizers under our conditions is given by

$$Q_{PS} = \frac{\lambda}{hc}\sigma\frac{\text{light beam power}}{\pi w_E^2} \tag{2}$$

where hc/λ is the energy of a photon, σ is the absorption cross-section of the PS in ethanol at the excitation wavelength, calculated from the measured molar absorptivity ϵ (see Table 3 for values) [46] and πw_E^2 is the cross-section surface of the Excitation Intensity Distribution (EID), see Table 3 and the section below. We get $Q_{MB} = 24.5 \times 10^6$ s^{-1} and $Q_{RB} = 3.6 \times 10^6$ s^{-1}.

Table 3 Parameters used to calculate detection limits: excitation wavelength (λ_{ex}), molar absorptivity (ϵ) and corresponding absorption cross-section (σ) at the excitation wavelength; singlet oxygen generation quantum yield in ethanol (ϕ_Δ); measured excitation power after the objective, during the excitation cycle of 200 pulses; radius of the excitation intensity distribution w_E as defined below and derived power density (light-beam power)/(πw_E^2).

	λ_{ex} nm	ϵ * M^{-1} cm^{-1}	σ $10^{-20}m^2$	ϕ_Δ [39, 47]	w_E μm	light-beam power mW	power density GW m^{-2}
MB	640	56725	2.169	0.52	1.53	3.06	0.35
RB	510	18384	0.703	0.68	1.22	0.93	0.20

* Determined by recording absorption spectra of the same solutions used to build the calibration curve.

Under the excitation frequency Q_{PS} a photosensitizer will absorb a photon into its excited singlet state, then will transition to its triple state by intersystem crossing with probability ϕ_Δ (see Table 3 for values). Given the PS triplet state lifetime τ_T, the probability p_T of finding a photosensitizer in its triplet state obeys $\dot{p}_T = Q_{PS}\phi_\Delta(1 - p_T) - p_T/\tau_T$, with $\dot{p}$ indicating the derivative of $p(t)$ with respect to time t. For $p_T(t = 0) = 0$ the solution is $p_T(t) = Q_{PS}\phi_\Delta\tau_T/(1 + Q_{PS}\phi_\Delta\tau_T) \times (1 - \exp[-t(1 + Q_{PS}\phi_\Delta\tau_T)/\tau_T])$. Thus, after a buildup time $\tau_T/(1+Q_{PS}\phi_\Delta\tau_T)$ the probability reaches a stationary state of value $1/(1+1/(Q_{PS}\phi_\Delta\tau_T))$. For MB, with a triplet state lifetime $\tau_T = 0.59$ μs, the probability p_T reaches a stationary state value $p_T = 0.88$ with a transition time of 69 ns, correspondingly roughly to 5 pulses. For RB, with $\tau_T = 0.49$ μs, the probability reaches a stationary state value $p_T = 0.55$ with a transition time of 223 ns, correspondingly roughly to 18 pulses.

In oxygenated enough solutions each triplet decay leads to the formation of a $^1O_2$. Thus, the number of $^1O_2$ per PS obeys $\dot{n}_O(t) = p_T(t)/\tau_T - n_O(t)/\tau$, where τ is the life

time of $^1O_2$ in the solvent. Integrating leads to $n_O(t) = \tau_T^{-1} \int_0^t p_T(s) \exp[-(t-s)/\tau] ds$ which, with the values determined above and τ=14.2 μs in ethanol, gives a number of $^1O_2$ per PS emitted after the 2.5 μs (200 pulses) excitation cycle $n_O = 40.4$ for MB and $n_O = 25.0$ for RB. After 60 seconds, each MB has thus produced 1.88×10^7 $^1O_2$, and each RB has lead to 1.90×10^7 $^1O_2$.

The radiative decay of $^1O_2$ in ethanol has been measured to occur with a probability of 4.8×10^{-6} [48]. One expects thus 24061 IR photons to be emitted by the 266 MB molecules in the confocal volume. Since 5325 IR photons were counted, the detection efficiency is ∼20 % for MB. For RB, one correspondingly expects an emission of 55437 photons by the 607 RB molecules. Here, the detection efficiency is ∼12 %. A collection efficiency of the order of or smaller than twenty percent is expected from the optical and detection geometry. Collection fraction angle is here given by $(1-\cos(\arcsin(1.05/1.5)))/2 = 0.17$, and typical losses by the optical elements (objective lenses, filters, dichroic mirror, ...) and the quantum efficiency of the detector can lead to further reductions.

The reported limit of detection (LOD) for singlet oxygen is specific to ethanol due to the solvent-dependent radiative rate constant. To estimate how this LOD scales with solvent, we calculated a value for water using established photophysical relationships. The detection sensitivity is inversely proportional to the phosphorescence quantum yield, $\phi_{em} = \tau/\tau_R$. Using literature values for water (τ = 3.6 μs, τ_R = 2.5 s) and our ethanol data (τ = 14.2 μ s, τ_R = 2 s), ϕ_{em} in water is approximately five times lower. Consequently, for a given photosensitizer like methylene blue, the minimum detectable number of $^1O_2$ molecules in water is estimated to be 8.5 10^6, representing an approximately fivefold increase compared to the LOD in ethanol.

Quantitative description of lifetime imaging for long-lived emission processes

We developed a quantitative description of lifetime imaging for long-lived emission processes such as those of NIR phosphorescence associated with single oxygen decay. This was achieved by expanding the well-established mathematical description of short-lived emission processes under confocal microscopy to account for the possibility of diffusion of the molecules excited into long lived states i.e. for probe diffusion between the location where a photon is absorbed and the location where a photon is emitted.

Standard fluorescence lifetime microscopy relies on the measurement of the number of photons emitted at time $t > -t_{ex}$ by fluorophores excited by laser pulses that follow a given excitation function $f(t)$ between times $-t_{ex} < t < 0$. Under these conditions, one typically measures for $t > 0$ a mono- or multi-exponential decay of the collected numbers of photons, with characteristic decay times of the order of nanoseconds. Under the appropriate conditions, excluding saturation effects, the spatial distribution of the excitation probability is described by the excitation intensity distribution (EID) [49], a function that can be approximated for practical purposes by a Gaussian of XY width w_E and Z depth $k_E w_E$:

$$EID(x,y,z) = \frac{2^{3/2}}{\pi^{3/2}} \frac{1}{w_E^3 k_E} \exp\{-2\frac{x^2+y^2}{w_E^2}\} \exp\{-2\frac{z^2}{w_E^2 k_E^2}\} \quad (3)$$

where k_E is the ratio between the longer (Z) and short (XY) widths of the Gaussian. The prolate ellipsoid surface defined by the $e^{-2} \simeq 0.135$ fraction of the function maximum at (0,0,0) has two short semi-axes (XY) of length w_E and one long (Z) axis of length $k_E w_E$.

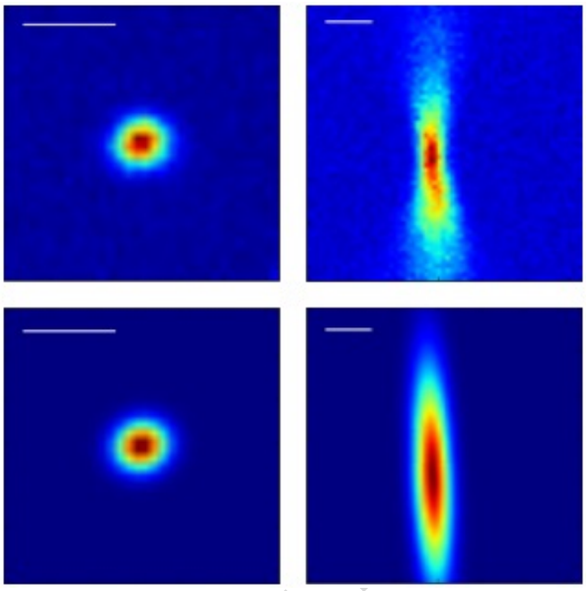

Fig. 8 Obtaining the Molecular Detection Function (MDF) from the light ($\lambda \geq 630$ nm) emitted by a fluorescent particle of sub-optical dimensions, collected with a 30X objective and a pinhole of 1.5 mm. Top row) XY and XZ intensity distributions; bottom row) the corresponding XY and XZ intensity distributions (MDF) extracted by Gaussian fits to the distributions in the top row, giving $w_M = 0.5$ μm and $k_M = 4$. Note that these values are larger than the Rayleigh/Abbe lateral resolution for our geometry ($\sim 0.61 \times \lambda/NA \sim 0.37$ μm). The scale bar is 1 μm in all images.

Decay of the excited states of the fluorophores results in the emission of photons, the emitted light being collected by the microscope light detectors in a typical confocal geometry with an efficiency described by the collection efficiency function (CEF). The CEF can also, for practical purposes, be approximated by a similar Gaussian function:

$$CEF(x,y,z) = \frac{2^{3/2}}{\pi^{3/2}} \frac{1}{w_C^3 k_C} \exp\{-2\frac{x^2+y^2}{w_C^2}\} \exp\{-2\frac{z^2}{w_C^2 k_C^2}\} \tag{4}$$

Excitation and emission at the same location. Thus, an immobile point-like unit-distribution of photons from fluorophores e xcited a t p osition (x', y', z') g ives, at detector position (x, y, z) a signal, also called the molecular detection function that reads:

$$MDF(x-x', y-y', z-z') = EID(x-x', y-y', z-z') \times CEF(x-x', y-y', z-z') \tag{5}$$

The MDF is also a Gaussian function with (XY) width w_M and (Z) width $k_M w_M$ given by:

$$\frac{1}{w_M^2} = \frac{1}{w_E^2} + \frac{1}{w_C^2} \quad \text{and} \quad \frac{1}{w_M^2 k_M^2} = \frac{1}{w_E^2 k_E^2} + \frac{1}{w_C^2 k_C^2} \tag{6}$$

The values of w_M and k_M can be measured for each microscope configuration by imaging the fluorescent light emitted by a very small fluorescent bead. Figure (8) shows XY and XZ cuts of the light distribution of a nanometer-size bead measured for our microscope with a 30X objective and the corresponding Gaussian fits of the intensity, according to Eq. 5. Under these conditions, one has $w_M = 0.5$ μm and $k_M = 4$ for the 1.5 mm pinhole.

Since w_M and k_M are the measurable quantities, it is convenient to introduce the relative extensions of the CEF and EID in the XY and Z directions, respectively $\alpha = w_C/w_E$ and $\beta = k_C w_C/(k_E w_E)$, so that one expresses all confocal volume dimensions in terms of the two known values w_M and k_M and the two numerical unknowns α and β. One has, for instance: $w_C = w_M\sqrt{1+\alpha^2}$, $k_C = k_M\sqrt{(1+\beta^2)/(1+\alpha^2)}$, $w_E = w_M\sqrt{1+\alpha^{-2}}$ and $k_E = k_M\sqrt{(1+\beta^{-2})/(1+\alpha^{-2})}$.

Note that the dimensions w_E and w_C of the excitation and of the collection volume respectively are always larger than the measurable value w_M of the molecular detection function. If both w_E and w_C were identical, then $\alpha = \beta = 1$ and one would have $w_E = w_C = 2^{1/2} w_M$.

With the notations introduced above, the MDF can be written as:

$$\begin{aligned} MDF(x-x', y-y', z-z') = \frac{2^3}{\pi^3} \frac{1}{w_M^6 k_M^2} \frac{1}{1+\alpha^{-2}} \frac{1}{(1+\beta^{-2})^{1/2}} \frac{1}{1+\alpha^2} \frac{1}{(1+\beta^2)^{1/2}} \\ \times \exp\{-2\frac{(x-x')^2+(y-y')^2}{w_M^2}\} \exp\{-2\frac{(z-z')^2}{w_M^2 k_M^2}\} \end{aligned} \tag{7}$$

Given the microscope MDF, one can compute the signal from an immobile fluorophore spatial distribution $O(x', y', z')$ with a generation rate $f(t')$ and single exponential decay time τ from:

$$\begin{aligned} I(x,y,z;t) = \int_{-t_{ex}}^{0} dt' \int dx' \int dy' \int dz' f(t')\ O(x', y' z') \\ \times \exp\{-\frac{t-t'}{\tau}\}\ MDF(x-x', y-y', z-z') \end{aligned} \tag{8}$$

In standard fluorescence lifetime measurements in solutions, the previous expressions also apply to mobile fluorophores. Indeed, even a fast fluorophore of diffusion coefficient $D \sim 10^{-8}$ m^{2}s^{-1} only explores during its lifetime $\tau \sim 10^{-9}$ s a distance $\sqrt{D\tau} \sim 3$ nm: in practice, a fluorophore excited in the confocal volume also emits

inside the confocal volume. Note also that, if the time required to generate a fluorescent species by an excitation pulse $P(t)$ is infinitesimally small, then $f(t) \sim P(t)$. In the case where intermediate processes are involved, such as those leading to singlet oxygen through a triplet state reaction with dioxygen, then $f(t)$ will be a time integral function of the laser intensity $P(t)$.

Mobile fluorophores: excitation at one location and emission at another. The previously described conditions for a fluorophore to be considered immobile might no longer be valid for long-lived processes such as those analysed in this paper. Indeed, for a typical singlet oxygen decay time τ of the order of 10^{-5} s in a solvent, the excited oxygen species travels over a distance of 300 nm, comparable to the width of the detection volume: a molecule excited in the confocal volume has a finite probability of escaping it before decaying. This is even more important for observations in the air where diffusion lengths up to a centimeter have been reported [50]. One thus needs to account for the mobility of the excited states in the expressions for the detected intensity. Given that under diffusion a molecule that was excited at position (x', y', z') at time t' has a probability $G_D(x''-x', y''-y', z''-z'; t-t')$ of being at a later time t at position (x'', y'', z''), with:

$$G_D(x''-x', y''-y', z''-z'; t-t') = \left(\frac{1}{4\pi D(t-t')}\right)^{3/2} \times \exp\{-\frac{(x''-x')^2+(y''-y')^2+(z''-z')^2}{4D(t-t')}\} \tag{9}$$

one can rewrite expression (8) for mobile species as

$$\overline{I(x,y,z;t)} = \int_{-t_{ex}}^{0} dt' \int dx' \int dy' \int dz' \int dx'' \int dy'' \int dz'' f(t') \times O(x', y'z')\; G_D(x''-x', y''-y', z''-z'; t-t') \exp\{-\frac{t-t'}{\tau}\} \times EID(x-x', y-y', z-z') \times CEF(x-x'', y-y'', z-z'') \tag{10}$$

Integration over all emission positions after diffusion (x'', y'', z'') leads to an expression formally identical to Eq. 8 but with a time dependent MDF that we note $\overline{MDF}$, where the width w_C^2 is replaced by $w_C^2 + 8D(t-t')$ and the width $k_C^2 w_C^2$ is replaced by $k_C^2 w_C^2 + 8D(t-t')$. With the notations introduced above, the molecular detection function for mobile species $\overline{MDF}$ can be written as:

$$\overline{MDF}\quad (x-x', y-y', z-z'; t-t') = \frac{2^3}{\pi^3} \frac{1}{w_M^6 k_M^2} \frac{1}{1+\alpha^{-2}} \frac{1}{(1+\beta^{-2})^{1/2}} \times \frac{1}{1+\alpha^2+8(t-t')/\tau_M} \frac{1}{[1+\beta^2+8(t-t')/(\tau_M k_M^2)]^{1/2}}$$

$$\times \exp\{-2\left(\frac{1}{1+\alpha^{-2}}+\frac{1}{1+\alpha^2+8\ (t-t')/\tau_M}\right)\frac{(x-x')^2}{w_M^2}\}$$
$$\times \exp\{-2\left(\frac{1}{1+\alpha^{-2}}+\frac{1}{1+\alpha^2+8\ (t-t')/\tau_M}\right)\frac{(y-y')^2}{w_M^2}\}$$
$$\times \exp\{-2\left(\frac{1}{1+\beta^{-2}}+\frac{1}{1+\beta^2+8\ (t-t')/(k_M^2\tau_M)}\right)\frac{(z-z')^2}{w_M^2 k_M^2}\} \quad (11)$$

where we introduced the confocal residence time $\tau_M = w_M^2/D$, *i.e.*, the time that the mobile probe spends in the confocal volume. In the limit where $\tau_M \to \infty$, the $\overline{MDF}$ reduces to the time-independent MDF as it should, since an immobile probe spends an infinite time in the confocal volume. Note that as defined here the $\overline{MDF}$ does not characterize the microscope geometry only, but accounts also for the diffusion of the excited species as well. The intensity $\overline{I(x,y,z;t)}$ collected by the microscope from time-decaying mobile species can thus be written in a form equivalent to Eq. 8

$$\overline{I(x,y,z;t)} = \int_{-t_{ex}}^{0} dt' \int dx' \int dy' \int dz' f(t')\ O(x',y',z')$$
$$\times \exp\{-\frac{t-t'}{\tau}\}\ \overline{MDF}(x-x', y-y', z-z'; t-t') \quad (12)$$

albeit with the time dependent $\overline{MDF}$ of Eq. 11. From Eq. 12 one can compute the image recorded by the microscope at time t from the photons emitted by mobile fluorophores excited by the fixed photosensitizer distribution $O(x',y',z')$. If the photosensitizers themselves are mobile, a time-dependent distribution $O(x',y',z',t')$ needs to be used.

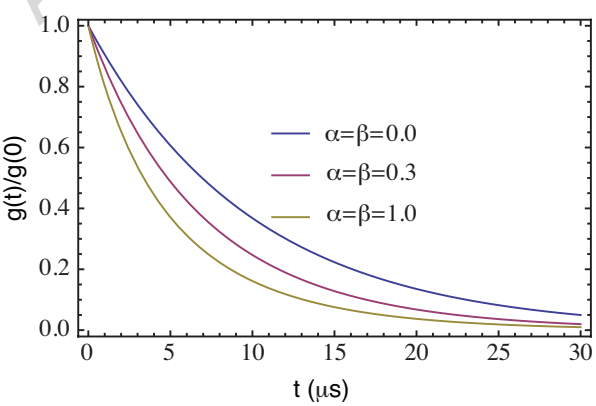

Fig. 9 Predicted normalised Diffusion-Biased Decay Functions $g(t)/g(0)$. Here plotted as a function of time 10^6 t (s), for species with decay time $\tau = 10^{-5}$ s in a typical situation where $\tau_M = 10^{-5}$ s, obtained from a diffusion coefficient $D \sim 10^{-8}$ m^2s^{-1} and a confocal distance $w_M = 3 \times 10^{-7}$ m. $\alpha = \beta = 0$ represents the expected exponential decay in the limit where diffusion does not play any role. $\alpha = \beta = 0.3$ corresponds to the case where the XY and Z dimensions of the CEF are 3 times smaller than those of the the EID. Maximum deviations are obtained when both ratios are equal to unity, $\alpha = \beta = 1$.

The mobility of the fluorophores thus induces two effects. The first effect is to increase the effective width of the MDF for mobile species, which is time dependent and larger than the corresponding one for spatially fixed fluorophores. This results in an additional spread of the light intensity detected by the microscope. The second effect is the reduction of the amount of collected photons due to the diffusion of the decaying species outside the confocal volume, which correspondingly changes the time evolution of the decay functions. If left uncorrected this effect will lead to wrong measurements of the phosphorescence decay times. We now provide quantitative descriptions of the these two effects.

How measured decaying functions are affected by the mobility of the photon-emitting species. For the practically relevant case of a bulk system where the fluorophores are homogeneously distributed everywhere, $O(x', y'z') = 1$, one gets, up to a global constant, a time decaying function ($t > 0$) corrected by diffusion that we denominate the diffusion-biased decay function or DBDF:

$$g(t) = \int_{-t_{ex}}^{0} dt' f(t') \left[1 + \frac{8(t-t')}{\tau_M(\alpha^{-1}+\alpha)^2}\right]^{-1} \times \left[1 + \frac{8(t-t')}{k_M^2 \tau_M(\beta^{-1}+\beta)^2}\right]^{-1/2} \exp\{-\frac{t-t'}{\tau}\} . \tag{13}$$

As expected, corrections to the (here) monoexponential bulk decay $\exp(-t/\tau)$ are significant if the molecules can diffuse, leaving the confocal volume on a timescale of the order of the decay time τ, *i.e.* if τ is comparable to or larger than τ_M. The DBDF in Eq. 13 also shows that the ratios of the horizontal (α) and vertical (β) extensions of the excitation (EID) and collection (CEF) volumes play a symmetric role for the decay function. For the limit of very small ratios α and β, the CEF is much smaller than the EID: molecules excited inside the CEF volume can leave it, but are compensated by the ones excited outside and entering it. For the limit of large ratios α and β the molecules excited in a small EID would all be collected by the much larger CEF. Note however that the observation geometry imposes several bounds to α and β, and that, for most relevant situations one has $\alpha, \beta \in [0.3 - 3]$.

Figure (9) displays the predicted decay curves for species with decay time $\tau = 10^{-5}$ s and a typical situation where $\tau_M = 10^{-5}$ s, obtained from a diffusion coefficient $D \sim 10^{-8}$ $m^2 s^{-1}$ and a confocal dimension $w_M = 3 \times 10^{-7}$ m. As the figure shows, the net effect of diffusion of the excited species out of the collection volume CEF is that the decay curves display apparent decay times smaller than the intrinsic unbiased values. Figure (10) displays $\tau_a/\tau = -g(0)dt/dg(t)|_{t=0}/\tau$, the ratio of the apparent decay time and the corresponding unbiased value, as a function of α (with $\beta = \alpha$), the ratios of the EID and CEF dimensions. As the figure shows for this particular case where $\tau_M = \tau = 10^{-5}$ s, due to the diffusion effects, the measured decay time τ_a can be as small as a half of the intrinsic time τ.

Despite the relative formal complexity of the integral in Eq. 1, simple operational principles can be given to properly interpret the measurements from homogeneous samples containing highly mobile fluorophores with long decay times. As Eq.1 shows,

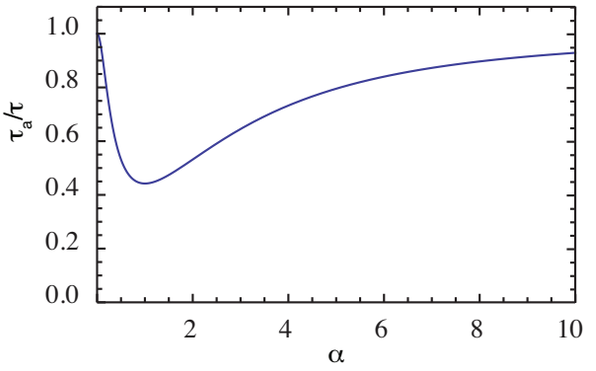

Fig. 10 $\tau_a/\tau = -g(0)dt/dg(t)|_{t=0}/\tau$, the ratio of the apparent decay time and the corresponding unbiased value, as a function of α (with $\beta = \alpha$). Here $\tau_M = \tau = 10^{-5}$ s.

the decay function depends : i) on the intrinsic decay time τ, ii) on the time $\tau_M = w_M^2/D$ that the probe spends in the MDF region, constructed from w_M the lateral dimension of the MDF and the probe diffusion coefficient D, iii) on the aspect ratio k_M of the ellipsoid describing the MDF and iv) on α and β, the relative lateral and vertical dimensions of the CEF and EID, $\alpha = w_C/w_E$ and $\beta = k_C w_C/(k_E w_E)$. The parameters w_M and k_M can be measured experimentally by determining the horizontal and vertical light distribution of fluorescent particles with nanoscopic dimensions. The parameters α and β cannot be measured, although they can in principle be computed with reasonable optical approximations. For a given probe, the intrinsic decay time τ and the associated diffusion coefficient D might be known or not. Thus, the instrument can be used both for determining the intrinsic decay time if the diffusion coefficient is known, or to determine the diffusion coefficient if the decay time is known. In both cases, the best approach is to first calibrate the instrument by measuring a well-known system in order to obtain the values of α and β and then use the calibrated configuration to perform the target measurements of either a decay time or a diffusion coefficient.

Light spread associated with the mobility of the emitting species. In order to illustrate the magnitude of light spreading on image acquisition due to the mobility of the emitting species, we rewrite and evaluate first Eq. 8 for immobile species with a radially distributed density on a sphere and then rewrite and evaluate Eq. 12 for mobile species for the case where light is absorbed by a radially distributed density of fluorophores (say a photosensitizer) on a sphere that then generate long lived mobile species (say singlet oxygen).

Under many practical circumstances the images are generated from all the photons collected after the excitation cycle stops, and one measures $I(x,y,z) = \int_0^\infty dt\ I(x,y,z;t)$. For immobile species on a sphere of radius R one thus has

$$I(\rho) = \int_0^{2\pi} d\phi \int_0^{\pi} \sin\theta d\theta \int_0^{R} r^2 dr\ O(r) \times MDF(\rho - r\cos\phi\sin\theta, -r\sin\phi\sin\theta, -r\cos\theta) \quad (14)$$

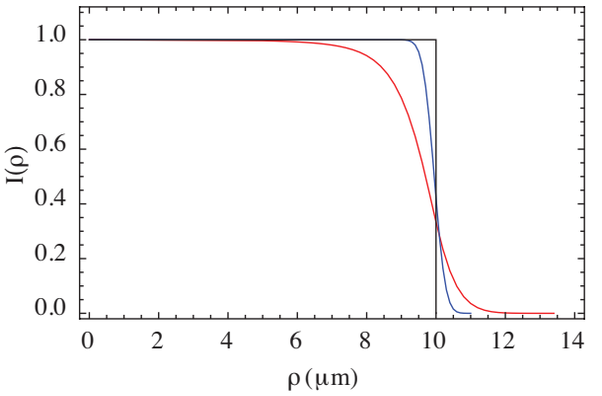

Fig. 11 Light-spreading due to diffusion of the emitting species. Additional light spread due to the mobility of long-lived emitting species for a sphere of radius $R = 10$ μm with the homogeneous radial fluorophore distribution $O(r) = 1$ for $r \leq R$, curve in black. In blue, the normalised radial intensity profile, expected from the fluorescence emitted by immobile species, detected by a confocal volume with lateral dimension $w_M = 0.5$ μm and asymmetry ratio $k_M = 4$. In red, the expected radial intensity distribution from the same confocal volume for the case of mobile species with decay time $\tau = 10$ μs, residence time $\tau_M = 0.1$ μs and relative extensions of the CEF and the EID $\alpha = \beta = 0.3$.

where ρ is a coordinate describing the radial component of the circularly symmetric image and $O(r)$ the radial density of fluorophores. In the simplest case the density $O(r)$ is a constant. The integral over ϕ can be performed analytically, leaving the evaluation of Eq. 14 to be performed by the double numerical integral:

$$\begin{aligned} I(\rho) = & \int_0^1 dp \int_0^R r^2 dr\ O(r) \\ & \times \left(\frac{2}{\pi}\right)^3 \frac{2}{w_M^3 k_M} \exp\left[-\frac{2}{w_M^2}(\rho^2 + r^2(1-p^2)) - \frac{2}{w_M^2 k_M^2}(r^2 p^2)\right] \\ & \times 2\pi I_0\left(\frac{4}{w_M^2}\rho r(1-p^2)^{1/2}\right) \end{aligned} \tag{15}$$

with I_0 the modified Bessel function of zero-th order. For mobile emitting species generated by sensitizers on a sphere one can equally write

$$\begin{aligned} I(\rho) = & \int_0^{2\pi} d\phi \int_0^{\pi} \sin\theta d\theta \int_0^R r^2 dr \int_0^{\infty} dt\ O(r) \\ & \times \overline{MDF}(\rho - r\cos\phi\sin\theta, -r\sin\phi\sin\theta, -r\cos\theta; t) \end{aligned} \tag{16}$$

with similar notations. After integration over ϕ the radial image profile can be obtained from the triple integral:

$$I(\rho) = \int_0^{\infty} dt \int_0^1 dp \int_0^R r^2 dr\ O(r)$$

$$\times \left(\frac{2}{\pi}\right)^3 \frac{2}{w_M^6 k_M^2} \frac{1}{1+\alpha^{-2}} \frac{1}{1+\alpha^2+8t/\tau_M} \frac{1}{(1+\beta^{-2})^{1/2}}$$
$$\times \frac{1}{(1+\beta^2+8t/(\tau_M k_M^2))^{1/2}} 2\pi I_0 \left(\frac{4}{w_M^2} \frac{1}{1+\alpha^{-2}} \frac{1}{1+\alpha^2+8t/\tau_M} \rho r (1-p^2)^{1/2}\right)$$
$$\times \exp\left[-\frac{2}{w_M^2} \frac{1}{1+\alpha^{-2}} \frac{1}{1+\alpha^2+8t/\tau_M} (\rho^2 + r^2(1-p^2))\right.$$
$$\left. - \frac{2}{w_M^2 k_M^2} \frac{1}{(1+\beta^2+8t/(\tau_M k_M^2))} (r^2 p^2)\right]$$
$$\times \exp[-t/\tau] \tag{17}$$

Figure (11) shows an example computed from Eq. 15 and Eq. 17 for a sphere that has an homogeneous radial distribution of sensitizers $O(r) = 1$ for $r \leq R$. It compares the intensity radial profiles $I(\rho)$ from images acquired with immobile (blue) and mobile (red) species, thus highlighting the additional light spreading induced by mobility.

Relative residuals plots for fittings shown in the main text

All signals presented an initial square-shaped spike, which corresponded mainly to fluorescence of the PS and lasted while the excitation was going on. This first part of the signal was discarded (time gating), and only the $^1O_2$ signal was fitted and used to generate images. We extract lifetimes as explained in the main text and here above. The corresponding residuals of the fits are displayed in Fig. (12).

Declarations

- Acknowledgments: MSB acknowledges ENS de Lyon for a visiting-professor fellowship. PDM acknowledges the John Simon Guggenheim Memorial Foundation.
- Funding: The *Fundação de Amparo à Pesquisa do Estado de São Paulo* (FAPESP) is gratefully acknowledged for grants 2013/07937-8 (CEPID Redoxoma), 13/11640-0 (IOLB fellowship); 15/10025-6 (CSP fellowship), 15/07508-5 (CM fellowship) and 15/07500-4 (APS fellowship). Also acknowledged the *Conselho Nacional de Desenvolvimento Científico e Tecnológico* (CNPq) grants 304350/2023-0 and 303831/2019-7, and the CAPES (*Coordenação de Aperfeiçoamento de Pessoal de Nível Superior*); CM, MSB and APS benefitted from CNRS support under the PICS07128 program.
- Conflict of interest/Competing interests: Authors declare no conflict of interest.
- Consent for publication: All authors agree with the publication.
- Data availability: All data is available in the manuscript and SI. Further information will be provided upon request.
- Author contribution: I.O.L.B: Methodology, Formal analysis, Investigation, Scientific Discussion, Writing, Review, Editing. C.M.M: Conceptualization, Supervision, Methodology, Theoretical formalism, Formal analysis, Investigation, Scientific Discussion, Writing, Review & Editing. A.P.S.: Methodology, Formal analysis, Investigation. C.S.P.: Methodology, Formal analysis, Investigation. H.C.J.: Methodology, Formal analysis, Investigation. P.D.M.: Scientific Discussion, Writing – Review &

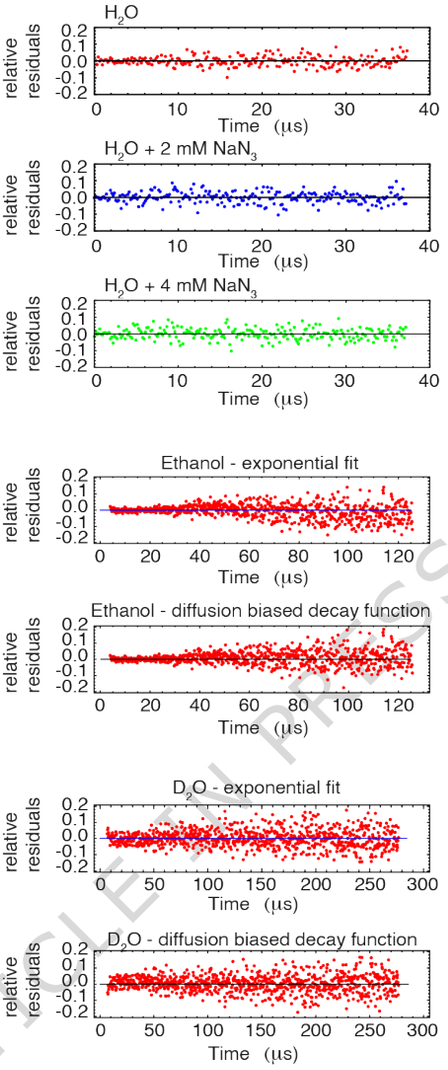

Fig. 12 Relative residuals plots for fittings shown in the main text

Editing, Visualization. M.S.B.: Conceptualization, Resources, Supervision, Scientific Discussion, Writing, Review, Editing.

References

[1] Kearns, D. R. Physical and chemical properties of singlet molecular oxygen. *Chemical Reviews* **71**, 395–427 (1971).

[2] Baptista, M. S., Cadet, J., Greer, A. & Thomas, A. H. Photosensitization reactions of biomolecules: Definition, targets and mechanisms. *Photochemistry and*

Photobiology **97**, 1456–1483 (2021). URL https://onlinelibrary.wiley.com/doi/abs/10.1111/php.13470.

[3] Foote, C. S. Mechanisms of photosensitized oxidation. *Science* **162**, 963–970 (1968).

[4] Baptista, M. *et al.* Type I and type II photosensitized oxidation reactions: Guidelines and mechanistic pathways. *Photochemistry and Photobiology* **93**, 912–919 (2017). URL https://onlinelibrary.wiley.com/Doi/full/10.1111/php.12716.

[5] Di Mascio, P. *et al.* Singlet molecular oxygen reactions with nucleic acids, lipids, and proteins. *Chemical reviews* **119**, 2043–2086 (2019).

[6] Mano, C. M. *et al.* Excited singlet molecular O_2 ($1\Delta g$) is generated enzymatically from excited carbonyls in the dark. *Scientific Reports* **4**, 5938 (2014).

[7] Klotz, L.-O., Kröncke, K.-D. & Sies, H. Singlet oxygen-induced signaling effects in mammalian cells. *Photochemical & Photobiological Sciences* **2**, 88–94 (2003).

[8] Nonell, S. & Flors, C. *Singlet Oxygen: Applications in Biosciences and Nanosciences Volume 1* (Royal Society of Chemistry, 2016).

[9] Nishinaka, Y., Arai, T., Adachi, S., Takaori-Kondo, A. & Yamashita, K. Singlet oxygen is essential for neutrophil extracellular trap formation. *Biochemical and biophysical research communications* **413**, 75–79 (2011).

[10] Chiarelli-Neto, O. *et al.* Generation and suppression of singlet oxygen in hair by photosensitization of melanin. *Free Radical Biology and Medicine* **51**, 1195–1202 (2011).

[11] Krieger-Liszkay, A. Singlet oxygen production in photosynthesis. *Journal of Experimental Botany* **56**, 337–346 (2004). URL https://Doi.org/10.1093/jxb/erh237.

[12] Stanley, C. P. *et al.* Singlet molecular oxygen regulates vascular tone and blood pressure in inflammation. *Nature* **566**, 548–552 (2019).

[13] Weu, A. *et al.* Oxygen-induced doping as a degradation mechanism in highly efficient organic solar cells. *ACS Applied Energy Materials* **2**, 1943–1950 (2019). URL https://doi.org/10.1021/acsaem.8b02049.

[14] Jiménez-Banzo, A., Sagristà, M. L., Mora, M. & Nonell, S. Kinetics of singlet oxygen photosensitization in human skin fibroblasts. *Free Radical Biology and Medicine* **44**, 1926–1934 (2008).

[15] Kuimova, M. K., Yahioglu, G. & Ogilby, P. R. Singlet oxygen in a cell: spatially dependent lifetimes and quenching rate constants. *Journal of the American Chemical Society* **131**, 332–340 (2009).

[16] Entradas, T., Waldron, S. & Volk, M. The detection sensitivity of commonly used singlet oxygen probes in aqueous environments. *Journal of Photochemistry and Photobiology B: Biology* **204**, 111787 (2020). URL http://www.sciencedirect.com/science/article/pii/S1011134419314551.

[17] Scholz, M., Dědic, R. & Hála, J. Microscopic time-resolved imaging of singlet oxygen by delayed fluorescence in living cells. *Photochem. Photobiol. Sci.* **16**, 1643–1653 (2017). URL http://dx.Doi.org/10.1039/C7PP00132K.

[18] Ogilby, P. R. Singlet oxygen: there is indeed something new under the sun. *Chem. Soc. Rev.* **39**, 3181–3209 (2010). URL http://dx.Doi.org/10.1039/B926014P.

[19] Scurlock, R. D., Nonell, S., Braslavsky, S. E. & Ogilby, P. R. Effect of solvent on the radiative decay of singlet molecular-oxygen (a1.DELTA.G). *Journal of Physical Chemistry* **99**, 3521–3526 (1995).

[20] Schlothauer, J., Hackbarth, S. & Röder, B. A new benchmark for time-resolved detection of singlet oxygen luminescence - revealing the evolution of lifetime in living cells with low dose illumination. *Laser Physics Letters* **6**, 216–221 (2009). URL https://Doi.org/10.1002%2Flapl.200810116.

[21] Ravanat, J.-L. & Cadet, J. Reaction of singlet oxygen with 2'-deoxyguanosine and DNA: Isolation and characterization of the main oxidation products. *Chemical Research in Toxicology* **8**, 379–388 (1995).

[22] Andersen, L. K., Gao, Z., Ogilby, P. R., Poulsen, L. & Zebger, I. A singlet oxygen image with 2.5 μm resolution. *The Journal of Physical Chemistry A* **106**, 8488–8490 (2002).

[23] Jarvi, M. T., Niedre, M. J., Patterson, M. S. & Wilson, B. C. Singlet oxygen luminescence dosimetry (sold) for photodynamic therapy: current status, challenges and future prospects. *Photochemistry and photobiology* **82**, 1198–1210 (2006).

[24] Li, B., Lin, H., Chen, D., Wilson, B. C. & Gu, Y. Singlet oxygen detection during photosensitization. *Journal of Innovative Optical Health Sciences* **6**, 1330002 (2013).

[25] Schlothauer, J. C., Falckenhayn, J., Perna, T., Hackbarth, S. & Röder, B. Luminescence investigation of photosensitizer distribution in skin: correlation of singlet oxygen kinetics with the microarchitecture of the epidermis. *Journal of biomedical optics* **18**, 115001–115001 (2013).

[26] Scholz, M., Dědic, R., Valenta, J., Breitenbach, T. & Hála, J. Real-time luminescence microspectroscopy monitoring of singlet oxygen in individual cells. *Photochemical & Photobiological Sciences* **13**, 1203–1212 (2014).

[27] Li, B., Lin, L., Lin, H. & Wilson, B. C. Photosensitized singlet oxygen generation and detection: Recent advances and future perspectives in cancer photodynamic therapy. *Journal of biophotonics* **9**, 1314–1325 (2016).

[28] Zebger, I. *et al.* Direct Optical Detection of Singlet Oxygen from a Single Cell. *Photochemistry and Photobiology* **79**, 319 – 322 (2004). URL https://doi.org/10.1562/RC-065R.1.

[29] Martins, W. K. *et al.* Parallel damage in mitochondria and lysosomes is an efficient way to photoinduce cell death. *Autophagy* **15**, 259–279 (2019).

[30] Hatz, S., Lambert, J. D. C. & Ogilby, P. R. Measuring the lifetime of singlet oxygen in a single cell: addressing the issue of cell viability. *Photochem. Photobiol. Sci.* **6**, 1106–1116 (2007). URL http://dx.doi.org/10.1039/B707313E.

[31] Andersen, L. K. & Ogilby, P. R. Time-resolved detection of singlet oxygen in a transmission microscope. *Photochemistry and Photobiology* **73**, 489–492 (2001).

[32] Breitenbach, T. *et al.* Photosensitized production of singlet oxygen: spatially-resolved optical studies in single cells. *Photochemical & Photobiological Sciences* **8**, 442–452 (2009).

[33] Jiménez-Banzo, A., Ragas, X., Kapusta, P. & Nonell, S. Time-resolved methods in biophysics. 7. Photon counting vs. analog time-resolved singlet oxygen phosphorescence detection. *Photochemical & Photobiological Sciences* **7**, 1003–1010 (2008).

[34] Niedre, M., Patterson, M. S. & Wilson, B. C. Direct near-infrared luminescence detection of singlet oxygen generated by photodynamic therapy in cells in vitro and tissues in vivo. *Photochemistry and photobiology* **75**, 382–391 (2002).

[35] Snyder, J. W., Skovsen, E., Lambert, J. D. & Ogilby, P. R. Subcellular, time-resolved studies of singlet oxygen in single cells. *Journal of the American Chemical Society* **127**, 14558–14559 (2005).

[36] Bregnhøj, M., Thorning, F. & Ogilby, P. R. Singlet oxygen photophysics: from liquid solvents to mammalian cells. *Chemical Reviews* **124**, 9949–10051 (2024).

[37] Tian, W. *et al.* Singlet oxygen phosphorescence lifetime imaging based on a fluorescence lifetime imaging microscope. *The Journal of Physical Chemistry A* **119**, 3393–3399 (2015).

[38] Junqueira, H. C., Severino, D., Dias, L. G., Gugliotti, M. S. & Baptista, M. S. Modulation of methylene blue photochemical properties based on adsorption at aqueous micelle interfaces. *Physical Chemistry Chemical Physics* **4**, 2320–2328 (2002).

[39] Wilkinson, F., Helman, W. P. & Ross, A. B. Rate constants for the decay and reactions of the lowest electronically excited singlet state of molecular oxygen in solution. An expanded and revised compilation. *Journal of Physical and Chemical Reference Data* **24**, 663–677 (1995).

[40] Turbay, M. B. E. *et al.* Effect of dye localization and self-interactions on the photosensitized generation of singlet oxygen by rose bengal bound to bovine serum albumin. *Journal of Photochemistry and Photobiology B: Biology* **141**, 275–282 (2014).

[41] Skovsen, E., Snyder, J. W. & Ogilby, P. R. Two-photon singlet oxygen microscopy: The challenges of working with single cells. *Photochemistry and photobiology* **82**, 1187–1197 (2006).

[42] McCabe, M. & Laurent, T. C. Diffusion of oxygen, nitrogen and water in hyaluronate solutions. *Biochimica et Biophysica Acta (BBA)-General Subjects* **399**, 131–138 (1975).

[43] Atenco-Cuautle, J. *et al.* Hasan, T. (ed.) *Rose bengal as a photosensitizer in the photodynamic therapy of breast cancer cell lines.* (ed.Hasan, T.) *17th International Photodynamic Association World Congress*, Vol. 11070, 11070A1. International Society for Optics and Photonics (SPIE, 2019). URL https://doi.org/10.1117/12.2525456.

[44] Snyder, J. W., Skovsen, E., Lambert, J. D., Poulsen, L. & Ogilby, P. R. Optical detection of singlet oxygen from single cells. *Physical Chemistry Chemical Physics* **8**, 4280–4293 (2006).

[45] Oliveira, C. S., Turchiello, R., Kowaltowski, A. J., Indig, G. L. & Baptista, M. S. Major determinants of photoinduced cell death: Subcellular localization versus photosensitization efficiency. *Free Radical Biology and Medicine* **51**, 824–833 (2011). URL https://www.sciencedirect.com/science/article/pii/S089158491100325X.

[46] Braslavsky, S. E. Glossary of terms used in photochemistry, (iupac recommendations 2006). *Pure and Applied Chemistry* **79**, 293–465 (2007).

[47] Redmond, R. W. & Gamlin, J. N. A compilation of singlet oxygen yields from biologically relevant molecules. *Photochemistry and photobiology* **70**, 391–475 (1999).

[48] Hasebe, N. *et al.* Absolute phosphorescence quantum yields of singlet molecular oxygen in solution determined using an integrating sphere instrument. *Analytical chemistry* **87**, 2360–2366 (2015).

[49] Enderlein, J. & Zander, C. *Theoretical Foundations of Single Molecule Detection in Solution*, Ch. 2, 21–67 (John Wiley & Sons, Ltd, 2003).

[50] Wang, K.-K. *et al.* Lifetime and diffusion distance of singlet oxygen in air under everyday atmospheric conditions. *Physical Chemistry Chemical Physics* **22**, 21664–21671 (2020).